Pore-level Foam Generation and Flow for Mobility Control in Fractured Systems

Jarand Gauteplass[1], Kuldeep Chaudhary[2], Anthony R. Kovscek[3] and Martin A. Fernø[1]

[1] Department of Physics and Technology, University of Bergen, Norway

[2] Jackson School of Geosciences, University of Texas at Austin, USA

[3] Department of Energy Resources Engineering, Stanford University, USA

Abstract

Pore-level foam generation, propagation, and sweep efficiency were visualized using a two-dimensional sandstone pore structure etched in a silicon wafer with accurate representation of grain shape, grain size and aspect ratios. *In situ* foam generation occurred by snap-off in the interior of the porous network (rectilinear snap-off) and at permeability discontinuities. Lamella creation by the two snap-off mechanisms identified here resulted in different foam textures. During foam injection for enhanced oil recovery, microvisual data revealed that the aqueous phase advanced as film flow along water-wet grains whereas discontinuous gas bubbles were located in the center of pores. Individual gas bubbles were mobilized by lamella displacement. Experimental results showed enhanced sweep efficiency in terms of greater pore occupancy by gas and larger contact area with displaced fluid for foam injection compared to continuous gas injection.

1. Introduction

Conventional oil production in fractured reservoirs is often characterized by large areas of unswept oil due to highly permeable thief zones dictating flow of the injected fluid. Gas injection, under miscible conditions provides excellent microscopic displacement efficiency, benefit from mobility control to mitigate gravity override, reduction in the impact of viscous instabilities, and achieves acceptable volumetric sweep in stratified reservoirs. Common techniques for enhancing oil recovery in heterogeneous and fractured systems by increasing sweep efficiency include Water-Alternating-Gas (WAG), hybrid-WAG, polymer gel treatment, and foam injection. Foam applications in the petroleum industry include well stimulation (Blauer and Kohlhaas, 1974, Gaydos and Harris, 1980, Norton and Hoffman, 1982) and gas diversion as an enhanced oil recovery (EOR) technique in formations (Ploeg and Duerksen, 1985, Hirasaki, 1989, Patzek and Koinis, 1990, Blaker et al., 1999).

Foam is defined as a gas dispersion within a continuous liquid phase. Individual gas bubbles are separated by thin liquid films, called lamellae, stabilized by surfactants at the gas/liquid interfaces (Kovscek and Radke, 1994). The main mechanisms behind foam generation are lamella division, lamella leave-behind and bubble snap-off (Mast, 1972, Ransohoff and Radke, 1988). In heterogeneous water-wet systems, where gas and liquid flow across sharp transitions in permeability, snap-off plays an important role (Roof, 1970, Falls et al., 1988, Rossen, 1999) and reduces foam flow perpendicular to stratification (Tanzil et al., 2002). Foam flow is shear-thinning and foam impedes the flow of gas in porous media and this reduction in gas mobility is proportionally greater in more permeable zones (Owete and Brigham, 1987). Foam is a proven technique for mobility control (Bernard and Holm, 1964, Holm, 1968, Lawson and Reisberg, 1980, Hirasaki and Lawson, 1985, Llave et al., 1990, Schramm, 1994, Rossen, 1996) by reducing gas mobility to improve macroscopic sweep efficiency and oil recovery. More recently, foam has been suggested to provide mobility control in fractures and systems featuring large permeability contrasts (Kovscek et al., 1995, Bertin et al., 1999, Nguyen et al., 2003, Yan et al., 2006, Fjelde et al., 2008, Li et al., 2010, Farajzadeh et al., 2010, Li et al., 2011, Buchgraber et al., 2012b, Haugen et al., 2012).

To use successfully foam as an EOR technique, foam behavior and flow properties must be accurately predicted at a variety of scales. Macroscopic foam properties such as viscous pressure drop and displacement efficiency heavily depend on microscopic processes such as foam generation and degradation. Experiments conducted on standard core samples and larger blocks within opaque systems do not allow direct observations of foam generation and propagation. Techniques such as computed tomography (CT) and magnetic resonance (MRI) enable *in situ* imaging, but do not yield sufficient pore-

scale spatial resolution needed to visualize lamella creation and degradation. In this study, we utilize two-dimensional etched-silicon micromodels for dynamic tracking of fluid interfaces at sub-pore scale as well as flow mechanisms and fluid propagation over several pores. We identify foam generation mechanisms and observe directly foam behavior in a fractured system. Furthermore, foam sweep efficiency is quantitatively compared to continuous gas injection (CGI) in a permeability transition zone.

2. Experimental Materials and Methods

2.1 Porous Media

Pore-scale foam generation and flow was experimentally visualized using 2D etched-silicon micromodels. **Figure 1** shows a schematic of the micromodel with ports for fluid injection and production (left) and a microscopic close-up of the etched pore network (right) with grain dimensions. Fluids are injected and produced through ports located in each corner of the device. An upstream and a downstream fluid distribution channel connect ports on one side of the micromodel and allows mostly linear flow through the pore network. These channels also introduce permeability contrasts.

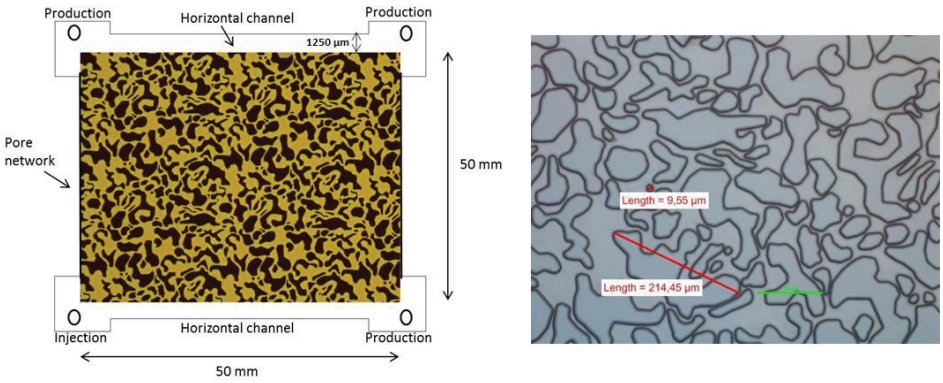

Figure 1 - Left: Micromodel system including injection/production ports, fluid distribution channels and pore network. The pore network is enlarged to see grains (black) and pore space (yellow) Right: Grain dimensions in the etched pore network varied between 10-215 µm (Gauteplass et al., 2013)

An idealized sandstone pore structure etched in the silicon wafer yields a 1:1 representation of grain shape, grain size and aspect ratios. This provides a realistic magnitude of capillary forces present in the system, which is a prominent parameter in fractured microfluidic systems. The models are water-wet due to a film of silicon dioxide coating the surfaces as a result of the bonding process. The wetting preference has been verified by contact angle measurements and imbibition tests (Gauteplass et al., 2013). The wetting fluid resided in pore corners, along the rough pore walls and as thin films coating flat surfaces (top and bottom), and maintained continuity even at low wetting saturation. A detailed fabrication procedure is described elsewhere (Buchgraber et al., 2012a). The pore network has more than $3.5x10^5$ pores distributed over a 5x5 cm^2 etched area, with a constant etching depth of 25 µm (Kovscek et al., 2007). Grain size ranges between 10-215 µm and the coordination number, describing pore accessibility, varies between 1-5. The dimension of the pore network appears to meet the representative elementary volume (REV) scaling requirements in 2D (Dullien, 1991).

2.2 Fluid Properties

Fluids and fluorescent additives are listed in **Table 1**. Fluorescent mixing ratios were designed to improve microvisual data and phase identification, as well as reduce photo bleaching and fluorescent additive retention in the pore space to a minimum.

Table 1 - Fluids used to study foam generation and displacement mechanisms

Phase	Fluid	Fluorescent	Mixing ratio	Emission spectrum peak
WATER	Deionized H_2O	Fluorescein	1:800 000	530 nm [a]
GAS	N_2 or Air	-	-	-
OIL	n-decane ($C_{10}H_{22}$)	Nile Red	1:100 000	635 nm [b]
SURFACTANT	1wt% BioTerge AS40	Fluorescein	1:800 000	530 nm [a]

[a] (Romanchuk, 1982)

[b] (Sigma-Aldrich, 2013)

2.3 Experimental Setup

Figure 2 shows a schematic of the experimental setup used to study displacement mechanisms and foam generation at the pore-scale. The centerpiece is an inverted Nikon Eclipse Ti-U microscope with four objective lenses for different scale resolution, neutral density filters, green and blue fluorescence filter cubes with individual exciter, emitter and dichroic beamsplitter, and a high-definition color camera capable of capturing images of 2560 x 1920 pixels with 16 bit RGB pixel depth. Gas was injected either with an injection pump or with a mass flow controller (MFC), and surfactant solution was injected using a syringe pump. Foam was pre-generated in a porous medium (sandstone or metallic sieve) upstream of the micromodel and visualized in a foam visualization cell prior to injection. A back-pressure regulator was used to reduce gas compressibility effects.

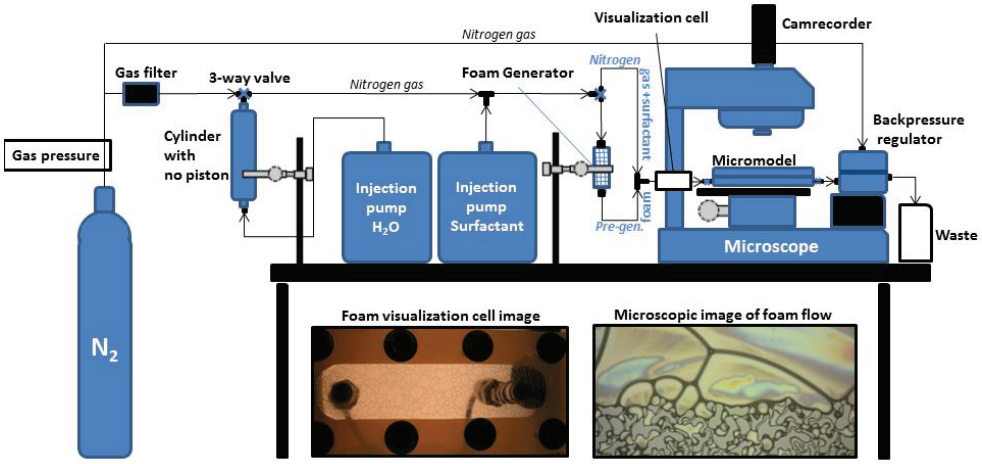

Figure 2 - The microfluidic setup included an inverted microscope fitted with a high-resolution camera, injection pumps, foam generator, flow visualization cell, micromodel and back-pressure regulator

2.4 Injection Schemes

Initial saturation: Micromodels were cleaned, vacuumed of liquid, and 100% saturated with gas. Then deionized water, mineral oil or aqueous surfactant solution were injected in series. In some cases the micromodels were partially saturated with water and oil by initiating a primary drainage in a fully water saturated model.

Gas flooding: Continuous gas injection (CGI) experiments were conducted by injecting a single gas phase into a liquid saturated micromodel at constant flow rate. The gas was filtered prior to entering the micromodel.

Foam injection: Varying fractions of gas and surfactant solution were flowing through a foam generator prior to entering the micromodel. Pre-generated foam texture was visualized in the flow visualization cell installed on the inlet side of the system. Foam quality was maintained by constant flow rate operations.

Processes described in section 3 are summarized in **Table 2**. Here, fluid initially saturating the micromodel, injection mode, gas fractional flow and total injection rate are listed.

Table 2 - Overview of injection processes and associated boundary conditions

Process	Initial Saturation	INJ mode	f_g	Q_{total} [cc/hr]	Figure #
Bulk foam generation	GAS	Pre-gen	0.95	4	3
Bulk foam generation II	WATER+OIL	Pre-gen	0.75	4	4
Layered foam generation	GAS	Pre-gen	0.8	4	5
Rectilinear snap-off	OIL	Pre-gen	0.8	4	6
Branch point foam generation	GAS	Pre-gen	0.8	4	7
Foam propagation	WATER+OIL	Pre-gen	0.75	4	8,10,11
Thinning of lamellae	GAS	Pre-gen	0.8	4	9
Sweep Efficiency	SURFACTANT	CGI	1	4	12
Sweep Efficiency	SURFACTANT	Pre-gen	0.95	4	12

3. Results and Discussion

Foam flow properties in porous media depend upon foam texture, that is, bubble density, shape and size. Foam texture is furthermore a function of foam generation and coalescence mechanisms as well as surfactant type and concentration. It is therefore important to understand pore-level foam behavior such as foam generation and propagation in order to describe macroscopic properties of foam flow. The first part of this chapter is devoted to mechanisms generating foam. The second part revolves around foam propagation and pore-level fluid distribution. Lastly, a comparison of sweep efficiency between foam and pure gas injection is performed.

3.1 Bulk Foam Generation

Foam was pre-generated during co-injection of gas and surfactant solution into a porous medium (metallic filter sieve, 40 μm, or a composite sandstone core plug) to generate foam. Foam texture, bubble size and bubble distribution were evaluated in a flow visualization cell prior to injection into the micromodel. The thickness of the foam visualization cell was 0.1 mm, and only a single bubble could occupy the thickness of the visualization cell. **Figure 3** shows foam texture after co-injecting gas and surfactant solution through a 40 μm metallic sieve at gas fractional flow, f_g = 0.95. With this gas fraction, the foam structure appeared as polyhedral with varying bubble sizes separated by thin lamellae. The aqueous solution consisted of deionized water and 1 wt% alpha olefin sulfonate (Bioterge AS40).

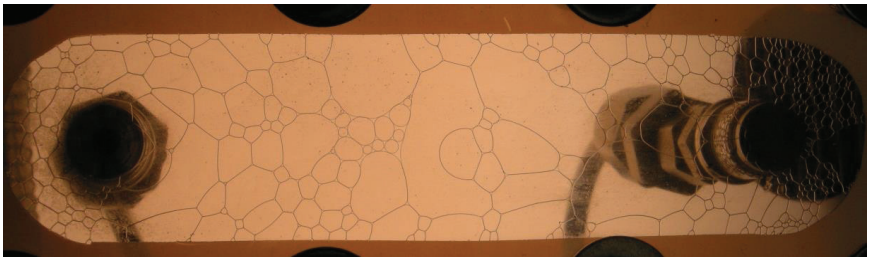

Figure 3 - Foam flowing from left to right in the visualization cell prior to entering the micromodel. At f_g = 0.95, a polyhedral foam structure was observed with varying bubble sizes separated by thin lamellae. Total flow rate is maintained at 4 cc/hr

Figure 4 shows bulk foam at f_g equal to 0.75 flowing from right to left in the fracture (horizontal distribution channel, see Fig 1) adjacent to an partially oil-filled matrix. Fluorescein was added to the surfactant solution to differentiate between the fluids present in the pore space. Gas and grains appear black. The pre-generated foam was defined as a two-dimensional bulk foam because the fracture aperture was larger than the gas bubble diameter. Bubbles have a polyhedral structure in the fractures. This bubble configuration is often described for foam flow in fractures (Kovscek et al., 1995, Buchgraber et al., 2012b).

Due to the relatively low gas fraction, thick liquid lenses were observed separating the gas bubbles. Average foam bubble diameter in the fracture was 219 μm. The lamellae separating each gas bubble were visualized and the average lamella thickness in bulk foam for f_g of 0.75 was 15 μm. The accumulations of liquids at the junctions of the lamella are called Plateau borders and could be identified in the image as bright areas where 3 lamellae met. The liquid pressure is lower in the Plateau border than in the lamella due to the curvature of the gas-liquid interface (Breward and Howell, 2002). Depending on the size and shape of bulk foam, 6 or 7 Plateau borders were associated with each gas bubble. With decreasing foam quality, capillary-suction pressure decreases as well and the Plateau borders can hold less liquid. This results in more circular foam bubble with relative thick lamella, as seen for gas fraction f_g = 0.75.

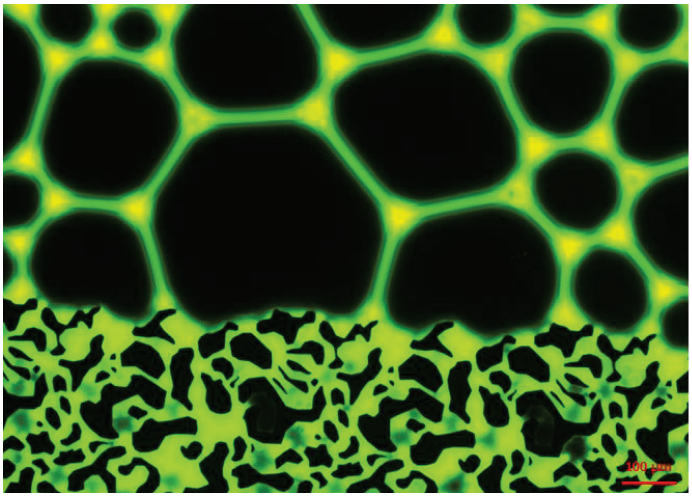

Figure 4 - Pre-generated bulk foam flowing from right to left in the upstream distribution channel. Fracture aperture exceeds gas bubble diameter. Foam structure is characterized by thick lamellae and circular bubbles due to high content of surfactant solution. Scale bar in lower right corner represents 100 μm

3.2 Permeability Discontinuity Foam Generation

Lamellae form in pore throats and are created by snap-off, lamella division or leave-behind. Our etched-silicon micromodels have pore bodies and pore throats yielding rectangular and square cross-sectional areas respectively. For snap-off mechanisms to occur in the current constrictions (width/height=1), capillary pressure must fall by about a factor of 2 compared to the capillary entry pressure (Lenormand et al., 1983). Capillary pressure reduction leading to snap-off can be ascribed to at least eight different mechanisms (Rossen, 2003, Chen et al., 2005). **Figure 5** shows foam generation by snap-off during simultaneous flow of gas and surfactant solution across a sharp permeability boundary. The region of low permeability (matrix) opens into a region of high permeability (fracture). Due to a greater index of refraction, the aqueous solution appears more dark grey compared to the gas. The two immiscible phases are separated by a thick black interface. Grains appear as isolated "islands" contoured by sharp pore walls of 25 μm perpendicular to flow direction. The gas bubble of interest is labelled "A" and is observed expanding from the center pore having a pore body radius, R_b = 24.45 μm and pore length, L = 67.93 μm, into a pore throat with an entry radius of R_c = 3.46 μm. The pore throat is initially filled with liquid and connects the center pore to the downstream channel. The lamella front (indicated with red arrows) is observed advancing in the pore throat, after 8.5 seconds the front reaches the downstream channel where several finely textured bubbles have accumulated from the same snap-off site. Capillary pressure decreases as the gas bubble expands. Between 8.5 and 11.4 seconds, the capillary pressure drops below the critical value for snap-off, and the wetting phase pinches off the non-wetting phase and forms a film bridging over the pore throat. The new foam bubble is labelled "A_2" and is generated yielding a bubble size equivalent of the pore throat volume. The average bubble size generated at the permeability boundary

was 21.5 µm, roughly 10 times smaller than pre-generated bubbles (Fig 4). The spontaneous rearrangement of wetting phase into a pore-spanning lens oriented perpendicular to the flow direction is shown at time step 11.4 seconds, located at the entry of the pore throat. In the last frame, after 19.9 seconds, the lamella/lens of the remaining bubble "A_1" is mobilized by a pressure gradient and displaced through the same pore throat, allowing further snap-off to occur. We observed repetitive foam generation at this specific site at sufficient wetting-phase content, consistent with other reports on capillary snap-off at a sudden permeability increase (Falls et al., 1988, Tanzil et al., 2002).

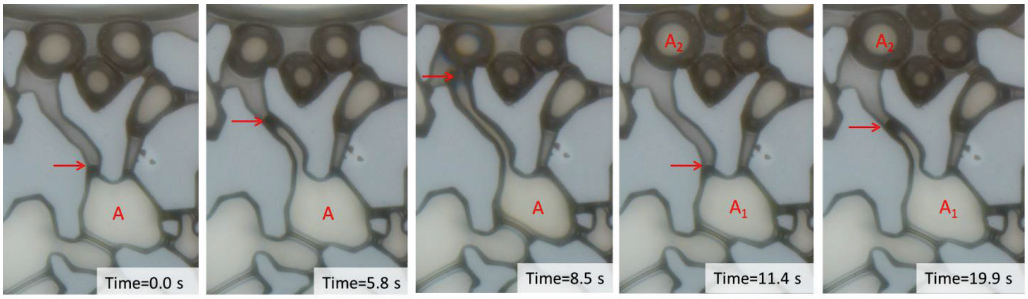

Figure 5 - Snap-off occurred repetitive in the permeability discontinuity zone between matrix and fracture. Flow direction is from bottom to top. The lamella front of bubble "A" was observed advancing in the pore throat towards the downstream channel and the subsequent snap-off divided gas bubble "A" into bubble A_1 and A_2. The lamella front is indicated with red arrows and time steps are presented in lower right corner

3.3 Pore-level Foam Generation

Foam generation within the interior of the pore network was investigated for both gas and oil saturated micromodels. During the lifetime of the foam injection both foam degradation and generation of new discrete bubbles were observed in the porous medium. Lamella collapse and subsequent merging of gas bubbles occurred more frequently in the presence of oil. **Figure 6** shows evidence of growing water films due to wetting phase accumulation followed by snap-off and forming of a new pore-sized foam bubble in an initially oil-filled micromodel. The areas of interest are marked with a red circle in the last frame and time step between the images is 2.7 seconds. From the first image to the last image, the water film is observed growing indicated by increased film thickness and increased film darkness (right circle). The snap-off mechanism occurs at the constriction (left circle) and the center pore is subsequently filled with a pore-spanning foam bubble. This process where the wetting phase pinches off the gas phase in the interior of the pore body, caused by capillary pressure fluctuations for individual bubbles, is defined as rectilinear snap-off (Chambers and Radke, 1991) or upstream snap-off (Huh et al., 1989). Consistent with Huh et al. (1989), we observed that bubbles generated by snap-off at the exit of the constriction were less coarse than bubbles created by upstream snap-off. Generally, smaller bubbles and finer-textured foam results in larger flow resistance (Ettinger and Radke, 1992). The rectilinear snap-off site has a pore throat to pore body ratio, $R_c/R_b = 0.3$ and a pore length to pore body ratio, $L/R_b = 5.7$.

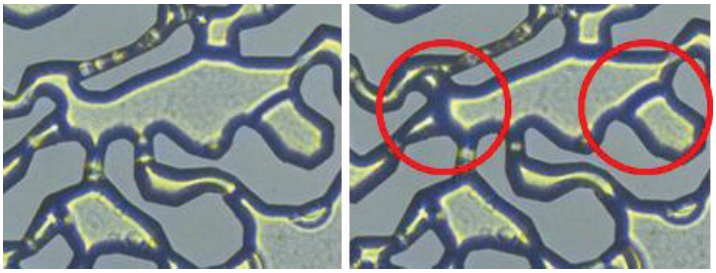

Figure 6 - Film thickening and subsequent snap-off occurring in the interior of the micromodel. Pre-generated foam at f_g = 0.8 was injected at constant flow rate of 4 cc/hr into an oil-filled micromodel at irreducible water saturation. Time taken between the two images is 2.7 seconds

In situ foam generation in the interior of the micromodel and in the permeability transition region, where the matrix opens into the downstream distribution channel, was identified as snap-off. In order to investigate if other foam generation mechanisms were active in the porous medium at current experimental conditions, a site yielding pore topological properties beneficial for lamella division was studied in detail. Lamella division requires a moving lamella and is therefore considered a secondary generation mechanism. Potential pore throat candidates for lamella creation by bubble subdivision, depends directly on coordination number of the pore bodies (Rossen, 2008). **Figure 7** shows a bubble labelled "A" advancing towards a branch point. The front of the gas bubble branches off in two directions, each growing slowly upwards in their respective pore throat as the bubble size exceeds current pore size. Both pore throats in this example were initially occupied by liquid. The front in the left pore throat was seen advancing more rapidly than in the right pore throat. The pore throat radius was $R_{c,l}$ = 3.84 µm and $R_{c,r}$ = 2.19 µm for respectively left and right pore throat. Furthermore, the center pore has a length, L = 71.77 µm and pore body radius, R_b = 24.73 µm. This resulted in a pore throat to pore body ratio, R_c/R_b = 0.2 and a pore length to pore body ratio, L/R_b = 2.9. In the last image frame, after almost 20 seconds, the whole gas bubble is displaced through the left pore throat followed by three smaller gas bubbles labelled "B", "C" and "D" (bubble train) being redistributed from elsewhere outside field of view. Several examples showed that when encountering a branched region, the lamella simply followed one pathway, usually where the pore throat radius was greatest, instead of dividing the lamella into two or more smaller bubbles.

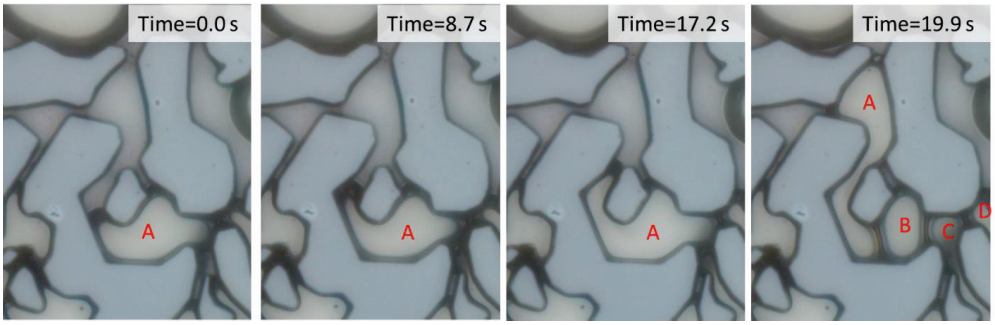

Figure 7 - Lamella movement in a branched region. Pre-generated foam at f_g = 0.8 was injected at constant flow rate of 4 cc/hr into an gas-filled micromodel. Bulk flow direction is from bottom to top in the image sequence, time steps are indicated in top right corner. Gas appear light grey, lamellae are black and grains are grey contoured by thin, dark lines

3.4 Foam Propagation and Fluid Transport

Dynamic tracking of fluid interfaces at pore-scale as well as fluid front movement at larger scale resolution was conducted using fluorescent additives to differentiate between the flowing phases. **Figure 8** shows an

interior area of the micromodel. Bulk flow direction is from bottom to top in this image. Discrete gas bubbles occupy larger pores, from where oil has been displaced, whereas surfactant solution is distributed along grain surfaces, in corners and as lamellae surrounding the gas bubbles. Time-lapse images revealed foam propagation, and subsequent oil displacement, as gas movement by lamella displacement and as continuous film flow of aqueous solution. Aqueous surfactant solution occupied smaller pores and pore throats whereas discontinuous gas bubbles were distributed in the center of larger pores. Furthermore, surfactant films coating matrix grains were identified in pores filled with gas, but not in pores filled with oil (Fig 8, Right). This is a consequence of the wetting preference of the porous medium. Thicker wetting films were observed in pores occupied by gas and water compared to pores filled with oil and water.

Breaking and reforming of gas bubbles occurred throughout the porous medium during foam injection. Foam coalescence strongly depends on the "limiting capillary pressure" in the pore system (Khatib et al., 1988), above this value merging of individual gas bubbles and coarsening of foam texture are expected. The limiting capillary pressure is a function of gas velocity, system permeability and surfactant type and concentration. The balance between foam generation and coalescence forces determines the size of foam bubbles (Kovscek et al., 2007). The majority of the confined foam within the micromodel had a bubble size equivalent to pore size and a bubble shape dictated by pore geometry.

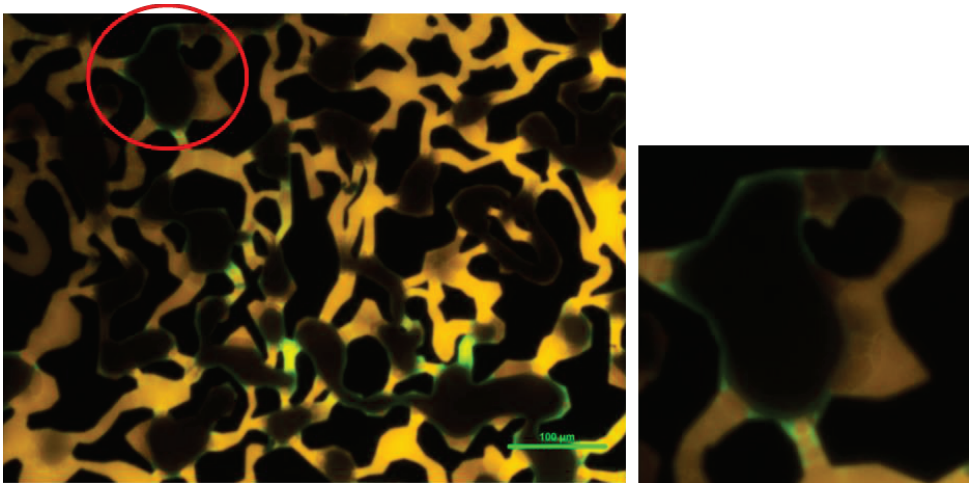

Figure 8 - Left: Fluid distribution during pre-generated foam injection at f_g equal to 0.75. Here, oleic phase dyed with Nile red appears orange in color, surfactant solution as green, gas as dark brown and grains as black. Scale bar in lower right corner is 100 µm. Right: Close-up of area marked with red circle in left image and shows pore-level film development in gas-filled pores versus oil-filled pores. Water films (green color) are identified in presence of gas

At macro-scale, foam was initially seen displacing oil co-current from the upstream fracture. Before oil was completely recovered from the fracture, matrix capillary threshold pressure was exceeded and gas diverted into the matrix. The water-wet nature of the porous medium led to aqueous solution spontaneously imbibing into the matrix from the fracture. This resulted in thinning of liquid lenses separating gas bubbles in the upstream fracture, as shown in **Figure 9.** Within 3 minutes, lamella thickness was reduced from 11.7 µm to 6.7 µm and the foam drainage resulted in coarsening of foam texture in the fracture. Note that these thicknesses include fluid in the Plateau border and so are apparent film thicknesses.

The process of film thinning is expected to continue until liquid pressure in the Plateau borders equals the liquid pressure in the matrix (Mast, 1972). After penetrating the matrix, foam immediately formed strong

preferential flow paths towards the downstream fracture. These preferential flow pathways were oriented orthogonal to the fracture flow direction and established a hydraulic connection between the two fractures (upstream and downstream distribution channels). The initial gas fingers grew in width and were subdivided into smaller branches, thus rapidly improving the sweep efficiency, and a piston-like displacement front at macro-scale was advancing towards the downstream channel. Oil was displaced both co-current and counter-current in the interior of the micromodel. As foam injection continued, gas bubble size decreased in the interior of the model and formation of emulsions occurred as the oil phase became finely divided, as shown in **Figure 10**. The forming of emulsions further facilitated an almost complete displacement of oil from the matrix. Enhanced foam generation and fluid diversion in the presence of microemulsions was previously reported by Huh et al. (1989).

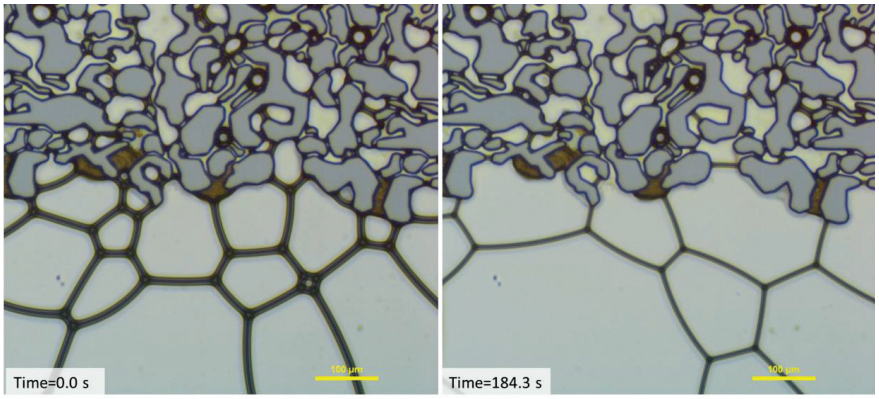

Figure 9 - Thinning of lamellae in upstream fracture during pre-generated foam injection at f_g = 0.8 at constant flow rate equal to 4 cc/hr into an gas-filled micromodel. Apparent lamella thickness was drained from 11.7 µm to 6.7 µm. Time and scale bar is included in the lower part of each image

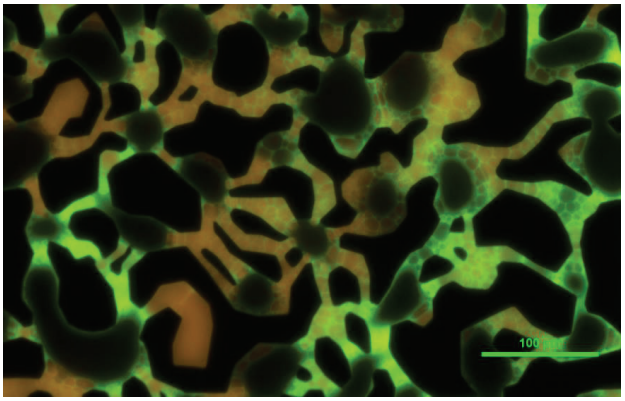

Figure 10 - Formation of an oil in water emulsion during pre-generated foam injection at f_g = 0.75 and flow rate of 4 cc/h. Oil dyed with Nile red appears orange/brown in color, surfactant solution as green, gas as dark brown and grains as black. Scale bar in lower right corner represents 100 µm

Figure 11 shows residual oil distribution within the matrix after foam injection. An almost complete displacement of oil was achieved; the pore space is mainly occupied by surfactant solution (green color) and individual gas bubbles (dark brown). A discontinuous oil blob (orange/brown color) is observed in a single pore with a coordination number of one, a so-called dead-end pore. In such a low capillary number and low Bond number system, capillary trapping of the non-wetting phase is a strong function of pore geometry (Chatzis et al., 1983). Residual oil in the micromodel was mainly observed trapped as singlet

and doublet structures. Only a few zones of residual oil were associated with several pore bodies. This implies that the oil was mainly trapped by bridge rupture (snap-off) and in dead-end pores, whereas bypassing occurred less frequently. Furthermore, surfactant solution is seen coating the grain surface and occupying narrow pore throats and some larger pores. Gas bubbles are distributed in the middle of the largest pores.

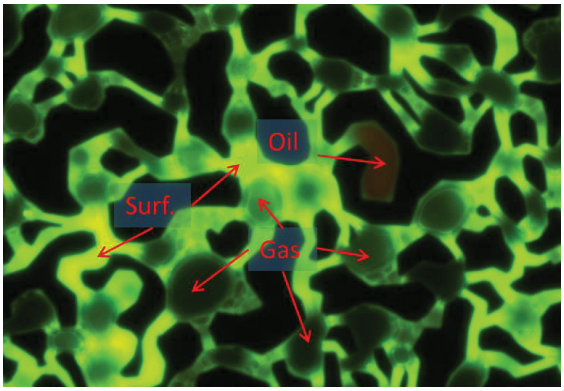

Figure 11 - Residual oil distribution after pre-generated foam injection at f_g = 0.75 and flow rate of 4 cc/h. Oil dyed with Nile red appears orange/brown in color, surfactant solution as green, gas as dark brown and grains as black

3.5 Recovery and Sweep Efficiency

Figure 12 compares the advance of gas (red) in the fracture and matrix initially filled with water and surfactant solution (blue) during gas injection (left column) and foam injection (right column). A back-pressure regulator was installed at the outlet to reduce compressibility effects. The fracture is located in the upper part of each image, and the matrix (lower part) consists of grains (white) and pore space. Color threshold has been applied to better distinguish between the three phases (gas, surfactant solution and grains) and to quantify sweep efficiency between pure gas and foam injection.

The injected gas during CGI (left column) displaced the aqueous solution from right to left in the fracture only, without any invasion to the liquid-filled matrix. The area swept by gas was determined by the capillary pressure and failure to establish a differential pressure drop across the fracture that exceeded the matrix threshold pressure. The injected gas during foam injection (right column) effectively displaced surfactant solution from the fracture, as observed during the pure gas injection. In contrast to CGI, gas also invaded the matrix to displace surfactant solution here. Over time, the number of foam bubbles in the matrix increased and the gas subsequently invaded pores with decreasing pore radius. In the last frame, foam occupied 87% of matrix pore volume and aqueous solution was only retained in the smallest pores and corners and as a wetting film along the matrix grains. Pre-generated foam injection showed evidence of a near-uniform gas distribution in a layered system at current experimental conditions. Foam also swept volumes of the micromodel outside the field of view, but this was not quantified.

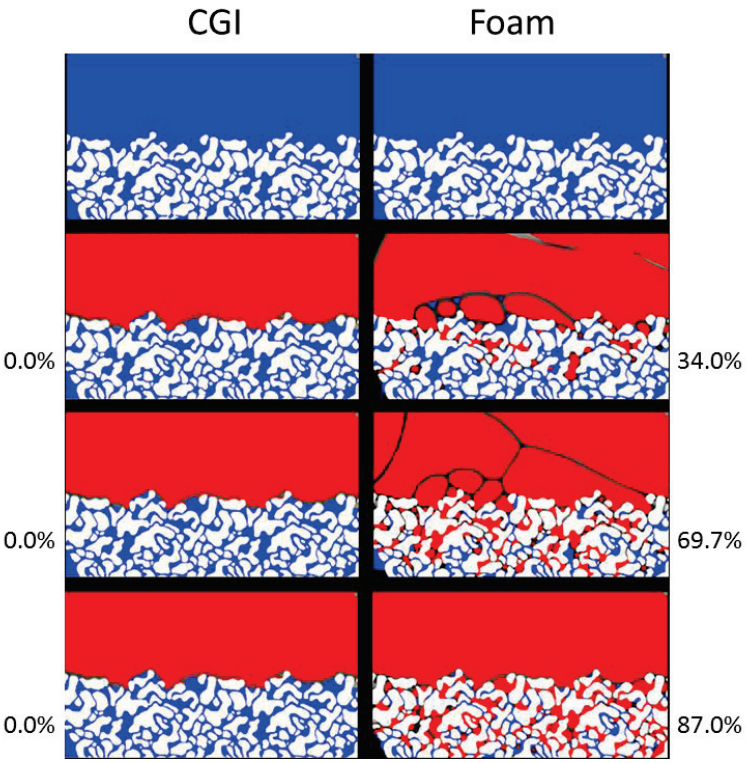

Figure 12 - Comparison of matrix sweep efficiency in a fractured system during gas injection (left column) and pre-generated foam injection (right column) at four different time steps. Gas is red, aqueous solution is blue and matrix grains are white. Number indicates % sweep efficiency of available matrix pore volume.

4. Conclusions

- Rectilinear snap-off and snap-off at permeability discontinuities were important mechanisms for *in situ* foam generation in our fractured systems. Foam generated at permeability discontinuities appeared more finely textured with smaller average bubble diameter compared to bubbles created by rectilinear snap-off. Bubble subdivision at branching pores was not observed at current experimental conditions
- Propagation of foam occurred as film flow for the aqueous solution and by lamella displacement for the gas phase. Residual oil was mainly trapped in single or double pore bodies by snap-off and in pore topological traps (dead-end pores)
- Foam injection in layered media successfully diverted gas from a high permeable fracture to a low permeable matrix. Matrix sweep efficiency within identical field of views were 0.0% and 87.0% for respectively CGI and foam injection

Acknowledgments

The authors are indebted to the Norwegian Research Council and the Petroleum Research School of Norway for financial support. Statoil, BP and ConocoPhillips are also thanked for their financial contribution.

References

BERNARD, G. G. & HOLM, L. W. 1964. Effect of Foam on Permeability of Porous Media to Gas.

BERTIN, H. J., APAYDIN, O. G., CASTANIER, L. M. & KOVSCEK, A. R. 1999. Foam Flow in Heterogeneous Porous Media: Effect of Cross Flow.

BLAKER, T., CELIUS, H. K., LIE, T., MARTINSEN, H. A., RASMUSSEN, L. & VASSENDEN, F. 1999. Foam for Gas Mobility Control in the Snorre Field: The FAWAG Project. Society of Petroleum Engineers.

BLAUER, R. E. & KOHLHAAS, C. A. 1974. Formation Fracturing with Foam. Society of Petroleum Engineers.

BREWARD, C. J. W. & HOWELL, P. D. 2002. The drainage of a foam lamella. *Journal of Fluid Mechanics***,** 379-406.

BUCHGRABER, M., AL-DOSSARY, M., ROSS, C. M. & KOVSCEK, A. R. 2012a. Creation of a dual-porosity micromodel for pore-level visualization of multiphase flow. *Journal of Petroleum Science and Engineering,* 86–87**,** 27-38.

BUCHGRABER, M., CASTANIER, L. M. & KOVSCEK, A. R. Microvisual Investigation of Foam Flow in Ideal Fractures: Role of Fracture Aperture and Surface Roughness. SPE Annual Technical Conference and Exhibition, 8-10 Oct 2012 2012b San Antonio, TX, US. SPE: Society of Petroleum Engineers.

CHAMBERS, K. T. & RADKE, C. J. 1991. Capillary Phenomena in Foam Flow Through Porous Media. *In:* MORROW, N. (ed.) *Interfacial phenomena in petroleum recovery.* Marcel Dekker Inc.

CHATZIS, I., MORROW, N. R. & LIM, H. T. 1983. Magnitude and Detailed Structure of Residual Oil Saturation.

CHEN, M., YORTSOS, Y. C. & ROSSEN, W. R. 2005. Insights on Foam Generation in Porous Media from Pore-Network Studies. *Colloids Surfaces A: Physicochem Eng. Aspects,* 256**,** 181-189.

DULLIEN, F. A. L. 1991. *Porous Media: Fluid Transport and Pore Structure*, Academic Press.

ETTINGER, R. A. & RADKE, C. J. 1992. Influence of Texture on Steady Foam Flow in Berea Sandstone.

FALLS, A. H., HIRASAKI, G. J., PATZEK, T. W., GAUGLITZ, D. A., MILLER, D. D. & RATULOWSKI, T. 1988. Development of a Mechanistic Foam Simulator: The Population Balance and Generation by Snap-Off.

FARAJZADEH, R., WASSING, L. B. M. & BOERRIGTER, P. M. 2010. Foam Assisted Gas Oil Gravity Drainage in Naturally-Fractured Reservoirs. *SPE Annual Technical Conference and Exhibition.* Florence, Italy Society of Petroleum Engineers.

FJELDE, I., ZUTA, J. & DUYILEMI, O. V. 2008. Oil Recovery from Matrix during CO2-Foam Flooding of Fractured Carbonate Oil Reservoirs. Society of Petroleum Engineers.

GAUTEPLASS, J., FOLLESØ, H. N., GRAUE, A., KOVSCEK, A. R. & FERNØ, M. A. 2013. Visualization of Pore-level Displacement Mechanisms During CO2 Injection and EOR Processes. *EAGE IOR - 17th European Symposium on Improved Oil Recovery* St. Petersburg, Russia.

GAYDOS, J. S. & HARRIS, P. C. 1980. Foam Fracturing: Theories, Procedures And Results. Society of Petroleum Engineers.

HAUGEN, Å., FERNØ, M. A., GRAUE, A. & BERTIN, H. J. 2012. Experimental Study of Foam Flow in Fractured Oil-Wet Limestone for Enhanced Oil Recovery.

HIRASAKI, G. J. 1989. The Steam-Foam Process. *Journal of Petroleum Technology,* 41**,** 449-456.

HIRASAKI, G. J. & LAWSON, J. B. 1985. Mechanisms of Foam Flow in Porous Media: Apparent Viscosity in Smooth Capillaries.

HOLM, L. W. 1968. The Mechanism of Gas and Liquid Flow Through Porous Media in the Presence of Foam.

HUH, D. G., COCHRANE, T. D. & KOVARIK, F. S. 1989. The Effect of Microscopic Heterogeneity on CO2-Foam Mobility: Part 1--Mechanistic Study.

KHATIB, Z. I., HIRASAKI, G. J. & FALLS, A. H. 1988. Effects of Capillary Pressure on Coalescence and Phase Mobilities in Foams Flowing Through Porous Media.

KOVSCEK, A. R. & RADKE, C. J. 1994. *Fundamentals of Foam Transport in Porous Media*, American Chemical Society.

KOVSCEK, A. R., TANG, G. Q. & RADKE, C. J. 2007. Verification of Roof snap off as a foam-generation mechanism in porous media at steady state. *Colloids and Surfaces A: Physicochemical and Engineering Aspects,* 302**,** 251-260.

KOVSCEK, A. R., TRETHEWAY, D. C., PERSOFF, P. & RADKE, C. J. 1995. Foam flow through a transparent rough-walled rock fracture. *Journal of Petroleum Science and Engineering,* 13**,** 75-86.

LAWSON, J. B. & REISBERG, J. 1980. Alternate Slugs Of Gas And Dilute Surfactant For Mobility Control During Chemical Flooding. Society of Petroleum Engineers.

LENORMAND, R., ZARCONE, C. & SARR, A. 1983. Mechanisms of the displacement of one fluid by another in a network of capillary ducts. *J . Fluid Mech.,* 135**,** 337-353.

LI, R. F., HIRASAKI, G. J., MILLER, C. A. & MASALMEH, S. K. 2011. Wettability Alteration and Foam Mobility Control in a Layered 2-D Heterogeneous System. Society of Petroleum Engineers.

LI, R. F., YAN, W., LIU, S., HIRASAKI, G. & MILLER, C. A. 2010. Foam Mobility Control for Surfactant Enhanced Oil Recovery.

LLAVE, F. M., CHUNG, F. T. H., LOUVIER, R. W. & HUDGINS, D. A. 1990. Foams as Mobility Control Agents for Oil Recovery by Gas Displacement. Society of Petroleum Engineers.

MAST, R. F. 1972. Microscopic Behavior of Foam in Porous Media. Society of Petroleum Engineers.

NGUYEN, Q. P., CURRIE, P. K. & ZITHA, P. L. J. 2003. Effect of Capillary Cross-Flow on Foam-Induced Diversion in Layered Formations. Society of Petroleum Engineers.

NORTON, M. G. & HOFFMAN, S. J. 1982. The Use of Foam in Stimulating Fractured California Reservoirs. Society of Petroleum Engineers.

OWETE, O. S. & BRIGHAM, W. E. 1987. Flow Behavior of Foam: A Porous Micromodel Study.

PATZEK, T. W. & KOINIS, M. T. 1990. Kern River Steam-Foam Pilots.

PLOEG, J. F. & DUERKSEN, J. H. 1985. Two Successful Steam/Foam Field Tests, Sections 15A and 26C, Midway-Sunset Field. Society of Petroleum Engineers.

RANSOHOFF, T. C. & RADKE, C. J. 1988. Mechanisms of Foam Generation in Glass-Bead Packs.

ROMANCHUK, K. G. 1982. *Fluorescein. Physiochemical factors affecting its fluorescence*.

ROOF, J. G. 1970. Snap-Off of Oil Droplets in Water-Wet Pores.

ROSSEN, W. R. 1996. *Foams in Enhanced Oil Recovery. Foams: Theory, Measurements and Applications*, Marcel Dekker.

ROSSEN, W. R. 1999. Foam Generation at Layer Boundaries in Porous Media.

ROSSEN, W. R. 2003. A critical review of Roof snap-off as a mechanism of steady-state foam generation in homogeneous porous media. *Colloids and Surfaces A: Physicochemical and Engineering Aspects,* 225**,** 1-24.

ROSSEN, W. R. 2008. Comment on "Verification of Roof snap-off as a foam-generation mechanism in porous media at steady state". *Colloids and Surfaces A: Physicochemical and Engineering Aspects,* 322**,** 261-269.

SCHRAMM, L. L. 1994. *Foams: Fundamentals and Applications in the Petroleum Industry*, American Chemical Society.

SIGMA-ALDRICH. 2013. http://www.sigmaaldrich.com/catalog/product/sigma/19123?lang=en&region=NO. [Accessed January 15 2013].

TANZIL, D., HIRASAKI, G. J. & MILLER, C. A. 2002. Mobility of Foam in Heterogeneous Media: Flow Parallel and Perpendicular to Stratification. *SPE Journal,* 7**,** 203-212.

YAN, W., MILLER, C. A. & HIRASAKI, G. J. 2006. Foam sweep in fractures for enhanced oil recovery. *Colloids and Surfaces A: Physicochemical and Engineering Aspects,* 282–283**,** 348-359.